Materials Horizons

ROYAL SOCIETY OF CHEMISTRY

COMMUNICATION

View Article Online
View Journal | View Issue

Cite this: *Mater. Horiz.*, 2025, **12**, 6804

Received 10th February 2025,
Accepted 27th May 2025

DOI: 10.1039/d5mh00251f

rsc.li/materials-horizons

Anion-mediated unusual enhancement of negative thermal expansion in the oxyfluoride of $PbTiO_3$†

Zhao Pan, *[ab] Yue-Wen Fang, [c] Sergey A. Nikolaev,[b] Lin Wu,[d] Jie Zhang,[a] Mengqi Ye,[a] Jin Liu, [a] Xubin Ye,[a] Xiao Wang, [a] Takumi Nishikubo,[be] Yuki Sakai,[be] Runze Yu,[f] Shogo Kawaguchi, [g] Nianpeng Lu,[a] Yoshihiro Kuroiwa,[c] Jun Chen, *[h] Masaki Azuma, *[be] Xianran Xing [h] and Youwen Long *[ai]

Materials featuring negative thermal expansion (NTE) properties are crucial for controlling overall thermal expansion. However, only a limited number of NTE materials are suitable as high-performance thermal expansion compensators owing to their small NTE magnitude and narrow NTE temperature range. $PbTiO_3$ is a typical perovskite-type (ABO_3) ferroelectric that also exhibits a unique NTE. While an enhanced NTE compared to pristine $PbTiO_3$ can be achieved in $PbTiO_3$-based ferroelectrics by improving their tetragonality *via* chemical substitutions at the A/B sites, the effect of anion substitution on the thermal expansion properties of $PbTiO_3$ has rarely been studied. Here, we report an oxyfluoride of $PbTiO_3$, as an O^{2-}/F^- solid solution with fluorine concentrations up to 10%, where $PbTiO_{3-x}F_x$ demonstrated a reduced tetragonality as a function of fluorine. Notably, for the first time, we observed a reduced tetragonality accompanied by an unusually enhanced NTE in the present $PbTiO_{3-x}F_x$ of $PbTiO_3$-based ferroelectrics, contrary to the previously reported enhanced NTE in $PbTiO_3$-based ferroelectrics. This unconventional phenomenon can be sufficiently understood considering the chemical bonds by the maximum entropy methods and first-principles calculations. This study not only extends the scope of NTE in $PbTiO_3$-based ferroelectrics but also expands the mixed-anion chemistry of the solid state.

New concepts

Materials with large negative thermal expansion (NTE) over a wide temperature range can serve as high-performance thermal expansion compensators. $PbTiO_3$ is a typical ferroelectric that also shows unique NTE. Technically, enhanced NTE could be achieved by improving the tetragonality (c/a) of $PbTiO_3$. While the most current modifications of the thermal expansion properties of $PbTiO_3$ have focused on the replacements of A/B-site cations, the effect of anion substitution on the NTE of $PbTiO_3$ has been rarely studied. Herein, for the first time we observed a reduced tetragonality accompanied by an enhanced NTE in the present oxyfluoride of $PbTiO_3$. This significantly differs from previously reported $PbTiO_3$-based NTE materials, where enhanced NTE occurred only in $PbTiO_3$-based materials with an enhanced tetragonality. The present study not only extends the scope of enhanced NTE in $PbTiO_3$-based ferroelectrics, but also demonstrates a new technique for introducing mixed anions to modify the NTE properties of functional NTE materials.

1. Introduction

Thermal expansion control is a long-standing issue in modern industrial applications including large structural components such as roads, railways, and bridges, as well as electronic devices such as multilayer chip capacitors and solid oxide fuel cells.[1–3] An undesired mismatch in the coefficient of thermal expansion (CTE) between different components in a device can induce several significant problems, such as performance deterioration, functional failure, or even cracking. Although most materials typically exhibit positive thermal expansion, only a few exhibit an unusual negative thermal expansion (NTE), in which the volume shrinks rather than expanding upon heating. NTE materials have undergone a significant development in the past few decades, originating from the phonon-related frameworks and

[a] *Beijing National Laboratory for Condensed Matter Physics, Institute of Physics, Chinese Academy of Sciences, Beijing, 100190, China. E-mail: zhaopan@iphy.ac.cn*
[b] *Laboratory for Materials and Structures, Tokyo Institute of Technology, 4259 Nagatsuta, Midori, Yokohama, 226-8503, Japan*
[c] *Centro de Fisica de Materiales (CFM-MPC), CSIC-UPV/EHU, Manuel de Lardizabal Pasealekua 5, 20018 Donostia/San Sebastian, Spain*
[d] *Graduate School of Advanced Science and Engineering, Hiroshima University, Higashihiroshima, Hiroshima 739-8526, Japan*
[e] *Kanagawa Institute of Industrial Science and Technology (KISTEC), 705-1 Shimoimaizumi, Ebina, Kanagawa 243-0435, Japan. E-mail: mazuma@msl.titech.ac.jp*
[f] *Center for High Pressure Science and Technology Advanced Research, Beijing 100193, P. R. China*
[g] *Research and Utilization Division, Japan Synchrotron Radiation Research Institute (JASRI), SPring-8, 1-1-1 Kouto, Sayo-cho, Sayo-gun, Hyōgo 679-5198, Japan*
[h] *Beijing Advanced Innovation Center for Materials Genome Engineering and Department of Physical Chemistry, University of Science and Technology Beijing, Beijing 100083, China. E-mail: junchen@ustb.edu.cn*
[i] *Songshan Lake Materials Laboratory, Dongguan, Guangdong 523808, China. E-mail: ywlong@iphy.ac.cn*

† Electronic supplementary information (ESI) available. See DOI: https://doi.org/10.1039/d5mh00251f

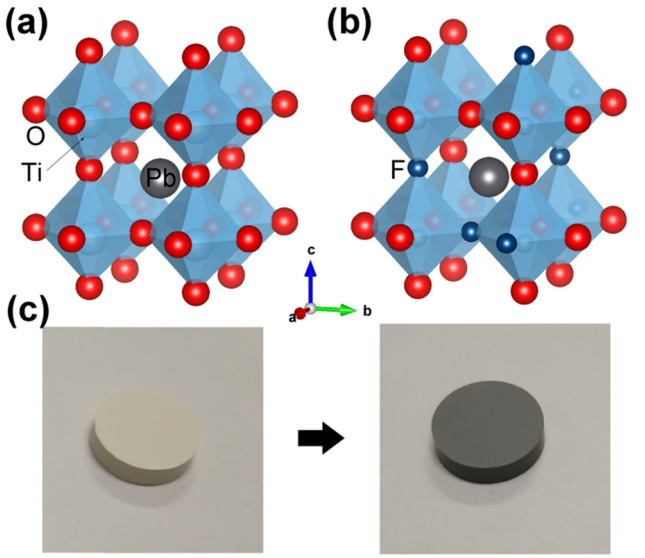

Fig. 1 The crystal structure of (a) $PbTiO_3$ and (b) oxyfluoride $PbTiO_{3-x}F_x$, where the oxygen anions (red spheres) are randomly replaced by fluoride anions (blue spheres). (c) The color changes before (yellow, $PbTiO_3$) and after (dark brown, $PbTiO_{2.8}F_{0.2}$) the fluoride insertion.

planar 2D materials,[4–7] magneto-volume effects in Invar alloys and manganese nitrides,[8–10] intermetallic charge transfer in $LaCu_3Fe_4O_{12}$ and $BiNiO_3$,[11,12] polar–nonpolar transition in polar perovskites,[13] and ferroelectrostriction in ferroelectrics.[14–16] The discovery of NTE has enabled controlling the overall thermal expansion of materials and is promising for constraining or eliminating thermal expansion *via* chemical modifications. However, the application of NTE materials is limited by the small magnitude of NTE and its narrow temperature range. Therefore, materials with a large NTE are important because a stronger NTE enables a more efficient counteraction of the positive thermal expansion within the composites.[17]

$PbTiO_3$ (PT) is a typical perovskite-type (ABO_3) ferroelectric (Fig. 1(a)) with a large tetragonal distortion (c/a = 1.064) and spontaneous polarization (P_S = 59 μC cm^{-2});[18] it also exhibits a unique NTE from room temperature (RT) to its Curie temperature (T_C = 490 °C) with an average volumetric CTE of $\bar{\alpha}_V = -1.99 \times 10^{-5}$ °C^{-1}.[19] By exploiting the flexible perovskite structure, the CTE of PT can be controlled by chemical substitutions or adjusting the microstructure.[2,20,21] In particular, an enhanced NTE compared to that of pristine PT can be achieved by increasing its tetragonality c/a.[2] For example, PT-based compounds with increased c/a ratios, such as 0.95PT-0.05$BiYO_3$ (c/a = 1.068, $\bar{\alpha}_V = -2.29 \times 10^{-5}$ K^{-1}, 300–800 K),[22] $Pb_{0.94}Cd_{0.06}TiO_3$ (c/a = 1.069, $\bar{\alpha}_V = -2.4 \times 10^{-5}$ K^{-1}, 300–743 K),[23] 0.95PT–0.05$BiGaO_3$ (c/a = 1.071, $\bar{\alpha}_V = -2.23 \times 10^{-5}$ K^{-1}, 300–768 K),[24] $PbTi_{0.9}V_{0.1}O_3$ (c/a = 1.077, $\bar{\alpha}_V = -3.76 \times 10^{-5}$ K^{-1}, 300–823 K),[15] and 0.4$PbTiO_3$–0.6$BiFeO_3$ (c/a = 1.165, $\bar{\alpha}_V = -3.92 \times 10^{-5}$ K^{-1}, 300–923 K),[25] exhibit enhanced NTE over a broad temperature range, compared to pristine PT. Conversely, compounds with lower c/a ratios, such as $PbTi_{0.95}Fe_{0.05}O_3$ (c/a = 1.056, $\bar{\alpha}_V = -1.49 \times 10^{-5}$ K^{-1}, 300–748 K),[26] 0.9$PbTiO_3$–0.1$Bi(Ni_{1/2}Ti_{1/2})O_3$ (c/a = 1.05, $\bar{\alpha}_V = -0.881 \times 10^{-5}$ K^{-1}, 300–798 K),[27] $Pb_{0.85}Sr_{0.15}TiO_3$ (c/a = 1.047, $\bar{\alpha}_V = -1.11 \times 10^{-5}$ K^{-1}, 300–673 K),[28] and $Pb_{0.95}La_{0.05}TiO_3$ (c/a = 1.040, $\bar{\alpha}_V = -1.02 \times 10^{-5}$ K^{-1}, 300–653 K),[19] show weakened NTE in a narrower temperature range compared to pristine PT.

To date, only a limited number of PT-based perovskites can exhibit an enhanced NTE compared to pristine PT, which occurs in those compounds with an improved tetragonality. Additionally, thus far, all the modifications of the NTE properties of PT-based ferroelectrics have focused on the chemical substitutions of the A and B sites, whereas the effect of anion substitution on NTE has rarely been studied. This could be due to the difficulty in sample preparation of the PT-based mixed-anion compounds. However, differences in the valences, electronegativities, and ionic radii of heteroanions are considered to greatly affect the crystal/electronic structure of PT, and therefore modify the NTE behavior.[29] Therefore, it is necessary to explore the effect of anion substitution on the NTE properties of PT, in order to further enrich the study of NTE in PT-based compounds. Herein, we have successfully prepared an oxyfluoride of $PbTiO_3$ by using a unique high-pressure and high-temperature (HTHP) synthesis method. Unexpectedly, we observed a reduced tetragonality accompanied by an unusual enhanced NTE in the present $PbTiO_{3-x}F_x$ compounds, which is in contrast to the previously reported enhanced NTE in $PbTiO_3$-based ferroelectrics with increased tetragonalities.

2. Results and discussion

A schematic diagram of the oxyfluoride of $PbTiO_3$ can be seen in Fig. 1(b). It shows the same tetragonal perovskite structure as that of pristine $PbTiO_3$. The $PbTiO_{3-x}F_x$ compounds contained a mixture of Ti^{3+}/Ti^{4+} (Fig. S1, ESI†), which is also present in other mixed-anion Ti-containing perovskites such as $ATiO_{3-x}H_x$ (A = Ba, Sr, Ca).[30–32] The color of the $PbTiO_{3-x}F_x$ powders changed from light yellow for pristine PT to dark brown for the oxyfluoride (Fig. 1(c)). Laboratory X-ray powder diffraction patterns showed that a phase-pure single perovskite structure can be obtained for $x \leq 0.2$. In contrast, noticeable impurities appeared for x = 0.3, indicating the solid solubility limit (Fig. 2a). The tetragonality of PT demonstrated a decreasing tendency with F substitution. The c/a ratios were 1.064, 1.058, and 1.056 for pristine PT, $PbTiO_{2.9}F_{0.1}$, and $PbTiO_{2.8}F_{0.2}$, respectively (see the inset of Fig. 2a). Notably, the Raman-active modes of A_1(1TO) and A_1(2TO), which are proportional to the order parameters of spontaneous polarization (P_S),[33] demonstrated a remarkable shift to lower frequencies as the F content increased (Fig. S2, ESI†), which was consistent with the reduced c/a. The reduced tetragonality can be related to the stronger electronegativity of F compared to that of O,[34] which is consequently responsible for the formation of ionic bonds between Pb/Ti and F, and the corresponding reduction in the covalent bonding between the cations and O.

To investigate the effect of F substitution on the thermal expansion properties of PT, the temperature dependence of the synchrotron X-ray powder diffraction (SXRD) patterns was studied for $PbTiO_{3-x}F_x$ (x = 0, 0.1, and 0.2), as shown in

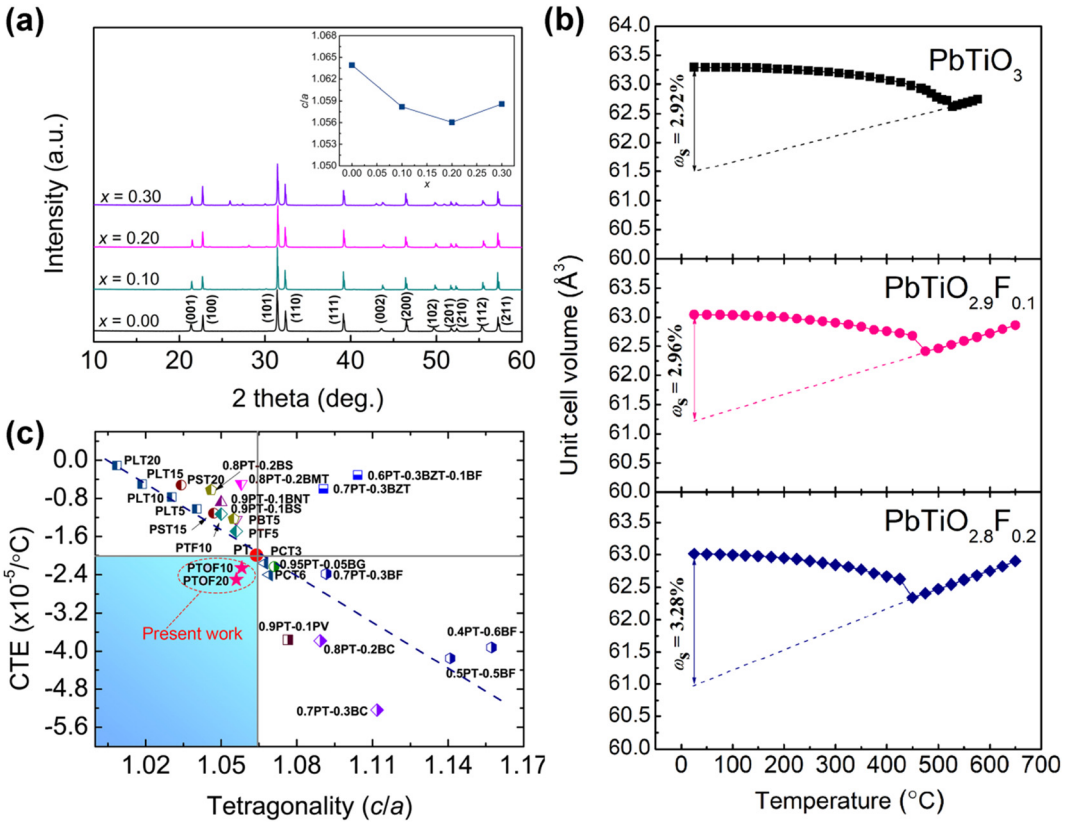

Fig. 2 (a) XRD patterns of $PbTiO_{3-x}F_x$ (x = 0, 0.1, 0.2, and 0.3) as a function of fluorine concentration, the inset shows the corresponding c/a ratio. (b) Temperature dependence of the unit cell volume for $PbTiO_{3-x}F_x$ (x = 0, 0.1, and 0.2). The error bars are smaller than the symbols. Schematic illustration of the SVFS (ω_S) is shown. (c) Average volumetric CTE as a function of c/a in the $PbTiO_3$-based ferroelectrics.[2] Among them, PLT100x is the abbreviation of $Pb_{1-x}La_xTiO_3$, PST100x indicates $Pb_{1-x}Sr_xTiO_3$, PTF100x stands for $Pb(Ti_{1-x}Fe_x)O_3$, PBT100x represents $(Pb_{1-x}Bi_x)TiO_3$, $(1-x)$PT–xBNT indicates $(1-x)$-$PbTiO_3$–$xBi(Ni_{1/2}Ti_{1/2})O_3$, PCT100x stands for $Pb_{1-x}Cd_xTiO_3$, $(1-x)$PT–xPV represents $(1-x)PbTiO_3$–$xPbVO_3$, $(1-x)$PT–xBF indicates $(1-x)PbTiO_3$–$xBiFeO_3$, and $(1-x)$PT–xBC indicates $(1-x)PbTiO_3$–$xBiCoO_3$, respectively.[2,13]

Fig. 2(b). Pristine PT demonstrated a nonlinear NTE from RT to its T_C with an average volumetric CTE of $\bar{\alpha}_V = -2.11 \times 10^{-5}$ $^\circ C^{-1}$. The CTE of the PT presented in this study slightly differs from the values reported in previous studies,[19] which may be related to the difference in the accuracy of the sample temperatures during the high-temperature XRD diffraction experiments. With the substitution by F, a slightly enhanced NTE with an average volumetric CTE of $\bar{\alpha}_V = -2.26 \times 10^{-5}$ $^\circ C^{-1}$ (RT $\sim$ 475 °C) was observed in $PbTiO_{2.9}F_{0.1}$. By increasing the concentration of F dopants, a remarkably enhanced NTE was observed in $PbTiO_{2.8}F_{0.2}$ with an average volumetric CTE of -2.50×10^{-5} $^\circ C^{-1}$ from RT to its T_C of 450 °C. Here, the slightly reduced T_C of $PbTiO_{2.9}F_{0.1}$ and $PbTiO_{2.8}F_{0.2}$ can be attributed to the reduced tetragonality. According to a previous study,[35] there is a strong relationship between the NTE and tetragonality in PT-based ferroelectrics (Fig. 2(c)). Generally, PT-based ferroelectric materials with a reduced tetragonality show a weakened NTE compared to pristine PT, whereas an enhanced NTE can only be achieved in materials with an enhanced tetragonality.[2] As summarized in Fig. 2(c), most ferroelectrics exhibit a reduced tetragonality and weakened NTE, whereas only a few systems exhibit an improved tetragonality and enhanced NTE. In this study, for the first time, we observed unusually enhanced NTE accompanied by a reduced tetragonality in the oxyfluoride $PbTiO_{3-x}F_x$, which significantly extends the scope of NTE in PT-based ferroelectrics.

Experimental and theoretical studies have suggested that ferroelectricity plays a crucial role in the NTE of PT-based ferroelectrics.[2] In the tetragonal ferroelectric phase, an increase in the unit-cell volume can be maintained by a large tetragonal distortion resulting from the P_S, whereas P_S and NTE disappear in the cubic paraelectric phase above T_C. A new physical concept of spontaneous volume ferroelectrostriction (SVFS, ω_S) has been recently proposed for ferroelectric NTE materials as a means to quantitatively evaluate the contribution of ferroelectricity to NTE. The SVFS is defined as follows,[14]

$$\omega_S = \frac{V_{exp} - V_{nm}}{V_{nm}} \times 100\%,$$

where V_{exp} and V_{nm} represent the experimental and nominal unit cell volumes, respectively, and V_{nm} can be estimated *via* extrapolation from the paraelectric to ferroelectric phase. A large value of ω_S indicates a strong ferroelectrovolume effect and enhanced NTE, whereas a small value indicates a weak NTE. Here, the ω_S values for pristine PT, $PbTiO_{2.9}F_{0.1}$, and $PbTiO_{2.8}F_{0.2}$ were 2.92%, 2.96%, and 3.28%, respectively, which are consistent with the

enhanced NTE observed in $PbTiO_{2.9}F_{0.1}$ and $PbTiO_{2.8}F_{0.2}$, respectively.

The hybridization between the A/B-site cations and oxygen is essential for the polar distortion and ferroelectricity in perovskite ferroelectrics.[36–38] To study the effect of F substitution on the ferroelectricity and thereby determine how it affects NTE, we investigated the temperature dependence of the electron density distribution over the temperature range where NTE occurs for PT, $PbTiO_{2.9}F_{0.1}$, and $PbTiO_{2.8}F_{0.2}$. The Rietveld refinements of the SXRD patterns at the tetragonal ferroelectric (27 and 327 °C) and cubic paraelectric (627 °C) phases of all the investigated samples were successfully performed based on the tetragonal *P*4*mm* and cubic *Pm*$\bar{3}$*m* space groups, respectively (Fig. S3, ESI†). Fig. 3 presents the electron density distributions of both the tetragonal and cubic PT, $PbTiO_{2.9}F_{0.1}$, and $PbTiO_{2.8}F_{0.2}$, which were determined using a combination of the maximum entropy method (MEM) and Rietveld refinement. The coordination number of the Ti atom was six in both the tetragonal and cubic phases. In the cubic phase of PT, $PbTiO_{2.9}F_{0.1}$, and $PbTiO_{2.8}F_{0.2}$ at 627 °C, the MEM electron densities at the six Ti–O/F bonds were equivalent and predominantly ionic. Conversely, in the tetragonal phases of PT, $PbTiO_{2.9}F_{0.1}$, and $PbTiO_{2.8}F_{0.2}$, the electron density around the Ti atom was highly anisotropic, which is attributed to the existence of the shorter and longer B–O bonds. The shorter Ti–O1/F1 bonds of the tetragonal PT (Ti–O1 bond in Fig. 3(a) and (b)), $PbTiO_{2.9}F_{0.1}$ (Ti–O1/F1 bond in Fig. 3(d) and (e)), and $PbTiO_{2.8}F_{0.2}$ (Ti–O1/F1 bond in Fig. 3(g) and (h)) at 27 °C and 327 °C were covalent, whereas the Ti–O1/F1 bonds of the cubic PT, $PbTiO_{2.9}F_{0.1}$, and $PbTiO_{2.8}F_{0.2}$ at 627 °C were more ionic (Ti–O1/F1 bond in Fig. 3(c), (f) and (i)). The Ti–O1/F1 covalent bonds in the tetragonal PT, $PbTiO_{2.9}F_{0.1}$, and $PbTiO_{2.8}F_{0.2}$ provide experimental evidence for the hybridization of the Ti 3d and O/F 2p orbitals. However, it should be noted that the Ti–O1 covalent bond of PT (minimum electron density (MED) = 1.33 $Å^{-3}$ at 27 °C) was stronger than the Ti–O1/F1 bonds of $PbTiO_{2.9}F_{0.1}$ (MED = 1.19 $Å^{-3}$ at 27 °C) and $PbTiO_{2.8}F_{0.2}$ (MED = 1.27 $Å^{-3}$ at 27 °C), indicating the higher covalency of the Ti–O1 bond in PT. These results indicate that the F substitution weakens the hybridization between Ti and O, resulting in the reduced tetragonality.

The covalent properties of the Pb–O bonds of PT, $PbTiO_{2.9}F_{0.1}$, and $PbTiO_{2.8}F_{0.2}$ were also investigated by calculating the corresponding MEM electron density distributions at 27, 327, and 627 °C, as demonstrated in Fig. S4 (ESI†). Similarly, the shorter Pb–O2 bonds in the tetragonal PT, $PbTiO_{2.9}F_{0.1}$, and $PbTiO_{2.8}F_{0.2}$ revealed a strong covalency in the tetragonal ferroelectric phase and became predominantly ionic in the high-temperature cubic paraelectric phase. It should be noted that the MED at the Pb–O2/F2 bonds of $PbTiO_{2.9}F_{0.1}$ (0.47 $Å^{-3}$ at 27 °C) and $PbTiO_{2.8}F_{0.2}$ (0.32 $Å^{-3}$ at 27 °C) was also smaller than that at the Pb/O2 bond in PT (0.59 $Å^{-3}$ at 27 °C), which is responsible for the weakened ferroelectricity as well as reduced tetragonality and T_C by the fluorine substitution of oxygen.

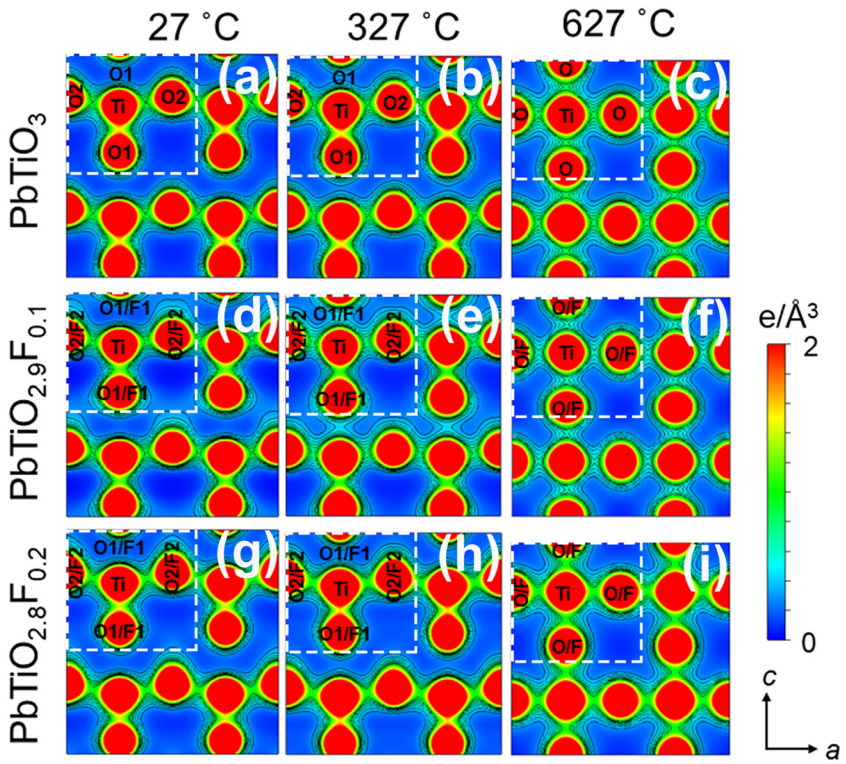

Fig. 3 Electron density distributions from the MEM calculations of $PbTiO_{3-x}F_x$ in the *ac* plane as a function of temperature in the tetragonal ferroelectric phase at 27 °C ((a), (d) and (g)), 327 °C ((b), (e) and (h)), and the cubic paraelectric phase at 627 °C ((c), (f) and (i)) for $PbTiO_3$, $PbTiO_{2.9}F_{0.1}$, and $PbTiO_{2.8}F_{0.2}$, respectively. Contours are shown from 0.3 to 0.6 $Å^{-3}$ with an interval of 0.1 $Å^{-3}$.

To further elucidate the microscopic origin of the unexpected enhancement of the NTE in $PbTiO_{3-x}F_x$, we revisited its structural and electronic properties using first-principles calculations. In this regard, we considered all the possible configurations with *F* dopants occupying different nonequivalent oxygen positions (either the out-of-plane 1b, or in-plane 2c sites, or both) and optimized each structure within a given supercell (Fig. S5, ESI†). Details regarding the calculations are provided in the ESI.† The calculated lattice parameters presented in Table SI (ESI†) for the undoped $PbTiO_3$ and the lowest-energy configurations of $PbTiO_{2.9}F_{0.1}$ and $PbTiO_{2.8}F_{0.2}$ (both having F ions at the 1b positions) indicate that the tetragonality *c*/*a* decreases as F doping increases, reproducing the experimentally observed changes in the crystal structure. Our results show that the introduction of F dopants slightly increases the in-plane lattice constant *a* but significantly compresses the unit cell in the out-of-plane *c* direction, which can be explained by the stronger covalency of the in-plane Ti–O bonds. Most importantly, we reveal that the off-centering displacements of the Ti atoms along the *c* axis tend to decrease upon doping for nearly all the considered configurations, leading to a change in the bonding characteristics of the doped Ti octahedra. These results are demonstrated in Fig. 4, where the calculated electron localization functions are shown for the undoped $PbTiO_3$ and the lowest-energy configurations of $PbTiO_{2.9}F_{0.1}$ and $PbTiO_{2.8}F_{0.2}$. The corresponding charge density maps of these structures are shown in Fig. S6 (ESI†). Owing to the strong off-centering displacements of the Ti atoms in the undoped $PbTiO_3$, the shorter out-of-plane Ti–O bond in the highlighted region features a predominantly covalent characteristic. Upon doping, the off-centering displacement of the F-bonded Ti ions decreased, and the bonding between Ti and F became essentially ionic, which was further enhanced by the increased concentration of F dopants. It should be noted that, owing to the vanishing off-centering displacements, the adjacent out-of-plane Ti–O bonds also changed and became more covalent. Similar features were observed for the other dopant configurations, as shown in Fig. S7 (ESI†). We observed a strong redistribution of the electronic density in the doped Ti octahedra, which was eventually responsible for the unit cell shrinkage and reduced tetragonality of $PbTiO_{3-x}F_x$. The observed redistribution driven by the local changes in the Ti–O/F octahedra can be understood by comparing the electron localization functions of the optimized and experimental structures, as shown in Fig. 4 and Fig. S8 (ESI†), respectively.

The overall effect of doping on $PbTiO_{3-x}F_x$ can also be determined by calculating the average Bader charges. As shown in Table SII (ESI†), the corresponding charge of Ti in the undoped $PbTiO_3$ was 2.14*e*, which was smaller than its nominally ionic charge (+4*e*) owing to the strong covalency between Ti and O, and further decreased to 2.13*e* for $PbTiO_{2.9}F_{0.1}$, and to 2.11*e* for $PbTiO_{2.8}F_{0.2}$, indicating a change in the bonding of the Ti octahedra. Although the stoichiometric $PbTiO_{3-x}F_x$ implies the mixing of the Ti^{4+} and Ti^{3+} oxidation states, which was also observed in the XPS experiments (see Fig. S1, ESI†), the

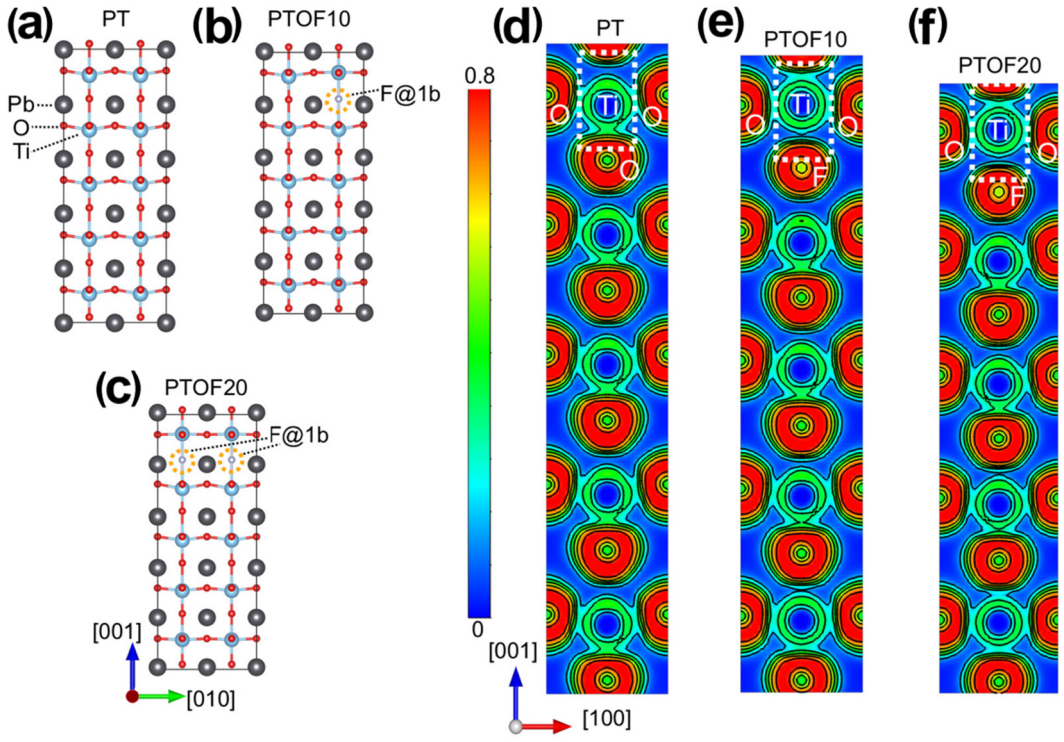

Fig. 4 Electron localization function for $PbTiO_{3-x}F_x$ as obtained from first-principles calculations for a 1 × 2 × 5 supercell. Optimized crystal structures of (a) undoped $PbTiO_3$ (PT), and the lowest energy configurations of (b) $PbTiO_{2.9}F_{0.1}$ (PTOF10) and (c) $PbTiO_{2.8}F_{0.2}$ (PTOF20). Electron localization function of (d) undoped $PbTiO_3$, the lowest energy configurations of (e) $PbTiO_{2.9}F_{0.1}$ and (f) $PbTiO_{2.8}F_{0.2}$. The white dashed rectangles highlight the F doped Ti octahedra.

resulting Bader charges demonstrated only a small change in the covalency, driven by the redistribution of the electronic density in the F-doped Ti octahedra.

Finally, previous studies by Chen *et al.*[39] showed that the polarization (or fundamentally, the polar displacements that break the inversion symmetry) is responsible for the NTE in ferroelectric PT-based compounds. Based on the calculated average off-centering displacements shown in Table SIII (ESI†), $\delta_M = d_X - d_M$, where M = Ti/Pb, X = O/F, and d is the atomic coordinate along the c axis, we conclude that the polar displacements of the metal ions decreased as the concentration of F dopants increased. This indicates that the ionic F dopants tend to reduce the polar displacements, which is consistent with our experimental data.

Control of thermal expansion is a fundamentally interesting topic in the field of NTE materials. Materials with strong NTE are very important, since they can be used to tailor the overall CTE of materials, or even realize the favorable zero thermal expansion. It is considered that the stronger the NTE is the more effective it is to counteract normal positive thermal expansion. $PbTiO_3$, a typical perovskite-type ferroelectric, also exhibits unique NTE properties. While much attention has been paid to modify the NTE properties of PT by replacing A-site Pb and/or B-site Ti cations, the effect of anion-site substitution on the NTE of PT remains unknown. Therefore, a feasible mixed anion control of thermal expansion of PT was proposed in the present study. Notably, enhanced NTE with reduced c/a was first realized in the present oxyfluoride of $PbTiO_3$. This is in contrast to previously reported $PbTiO_3$-based NTE materials, where enhanced NTE occurred only in $PbTiO_3$-based materials with an enhanced tetragonality. The anion-mediated enhanced NTE therefore demonstrates a new technique for realizing large NTE in PT-based perovskites, as well as provides a new way for the design of high-performance NTE materials.

3. Conclusion

In summary, our results suggest that the enhanced negative thermal expansion of PT-based ferroelectrics, which generally occurs in compounds with an improved tetragonality, can also be achieved in mixed-anion-substituted PT with a reduced tetragonality. This unconventional phenomenon can be understood considering the chemical bonds, which are crucial for the ferroelectric activity of PT-based compounds, as well as their thermal expansion properties. The present study greatly extends the scope of the NTE in PT-based ferroelectrics and highlights enhanced NTE materials.

4. Experimental section

4.1. Sample preparation

Polycrystalline samples of $PbTiO_{3-x}F_x$ (x = 0, 0.10, 0.20, and 0.30) were synthesized by a high-temperature (HT) and high-pressure (HP) method. The raw materials of PbO (99.99%, RARE METALLIC), PbF_2 (95.0%, FUJIFILM Wako Pure Chemical), and TiO_2 (99.99%, RARE METALLIC) were mixed in a stoichiometric ratio. The mixtures were sealed in a platinum capsule with a diameter of 3.6 mm and a height of 5.0 mm, followed by the HT-HP treatment at 8 GPa and 1200 °C for 30 min using a cubic anvil-type apparatus. After HT-HP synthesis, the samples were carefully ground and annealed at 400 °C for 1 h, then slowly cooled to room temperature (RT).

4.2. Structural characterization

The crystal structures for all the samples have been characterized by means of laboratory X-ray powder diffraction (XRD) performed on a Bruker D8 ADVANCE diffractometer. The synchrotron X-ray diffraction (SXRD) data were collected at the BL02B2 beamline of SPring-8 with a light wavelength of ~0.42 Å. The detailed structure analysis was performed with the same initial model as that of $PbTiO_3$ (space group *P4mm*, No. 99) by the Rietveld method using the FullProf software.[40] The oxidation states of Titanium were analyzed by X-ray photoelectron spectroscopy (XPS, AXIS Ultra DLD, Kratos, Japan). The Raman scattering spectra were collected on a Raman spectrometer (WITec Alpha 300R) at room temperature.

4.3. Theoretical calculations

The Fist-principles calculations were performed in the Vienna *Ab initio* Simulation Package (VASP),[41,42] and PBEsol, a revised Perdew–Burke–Ernzerhof generalized gradient approximation for improving the equilibrium properties of densely-packed solids,[43] was used as the exchange–correlation functional. This method has been successfully applied to study polar materials in our previous works.[44,45] In our calculations we used a 1 × 2 × 5 superlattice and a 12 × 6 × 2 k-point mesh. All considered dopant configurations of $PbTiO_{3-x}F_x$ were optimized, where the lattice vectors and atomic coordinates were both fully relaxed with the force convergence criterion set to 10^{-2} eV Å^{-1}. The cutoff energy was set to 500 eV. We did not take into account the effect of electronic correlations for the Ti d shell, which is expected to give only minor quantitative changes to the presented results.

Since there are two nonequivalent crystallographic oxygen sites in the unit cell of tetragonal $PbTiO_3$ (*P4mmm*), corresponding to the Wyckoff 1b (1/2, 1/2, z) and 2c (1/2, 0, z) positions, the F ions may occupy either the 1b (F@1b) or 2c (F@2c) sites, or both (F@1b&2c). Hence, in order to simulate $PbTiO_{2.9}F_{0.1}$ and $PbTiO_{2.8}F_{0.2}$ we considered all possible doped configurations within the 1 × 2 × 5 supercell. Specifically, there are three nonequivalent configurations for $PbTiO_{2.9}F_{0.1}$, and thirty-five nonequivalent configurations for $PbTiO_{2.8}F_{0.2}$. The relative energy profile for all possible configurations of $PbTiO_{2.9}F_{0.1}$ is shown in Fig. S4(b) (ESI†), in which the configuration 0 with F@1b is set to zero as the reference energy. The corresponding crystal structures of $PbTiO_{2.9}F_{0.1}$ with F@1b and F@2c are shown in Fig. S4(c) and (d) (ESI†), respectively. The relative energy profile for $PbTiO_{2.8}F_{0.2}$ is shown in Fig. S4(e) (ESI†), in which the configuration 2 with F@1b is set as the zero energy. The crystal structures of the respective lowest energy configurations

with F@1b, F@2c, and F@1b&2c of $PbTiO_{2.8}F_{0.2}$ are shown in Fig. S4(f), (g) and (h) (ESI†), respectively.

To investigate the bonding properties, we have calculated the electron localization function (ELF). A value of ELF close to one means the possibility to find a pair of electrons at a specific position is relatively high, a zero value implies that no electron can be found at the location or the electrons are fully delocalized; and ELF close to one-half represents the electron-gas like pair distribution.[46,47] Taking into account that the actual occupation of F dopants in the experiment can be at the Wyckoff 2c sites, we comparatively show the ELF distributions for $PbTiO_{2.9}F_{0.1}$ with F@1b and F@2c in Fig. S5 (ESI†), where the strong ionic features of the Ti–F bond are observed in both cases.

The calculated Bader charges of $PbTiO_3$, $PbTiO_{2.9}F_{0.1}$, and $PbTiO_{2.8}F_{0.2}$ are presented in Table SII (ESI†). Since the Bader charges of the Ti ions are reduced almost universally with the increased concentration of F dopants, only the averaged values are shown. The calculated off-centering polar displacements of Pb and Ti with respect to the anions, $\delta_M = d_X - d_M$, where M = Ti/Pb, X = O/F, and d is the atomic coordinate along the c axis, are listed in Table SIII (ESI†).

Our calculations are robust independent of the electron correlations. To investigate the Hubbard U effect, we used Dudrav *et al.*'s method to perform DFT+U calculations.[48] The density of states of DFT are compared with those from the DFT+U (U = 1, 2, and 3 eV) calculations in Fig. S9 (ESI†). Our calculations show that neither the Ti–anion hybridizations linked to negative thermal expansion nor the band gap change noticeably when the U correction is applied.

Author contributions

The project was conceived by Z. P., J. C., M. A., and X. R. X. Samples were prepared by Z. P., who performed the SXRD measurements with help from J. Z., X. B. Y., T. N., Y. S., and S. K. The XPS measurements were conducted by R. Z. Y. The Raman spectral experiments were conducted by M. Q. Y, J. L., and N. P. L. The MEM calculations were performed by L. W., guided by Y. K. The theoretical calculations were carried out by Y.-W. F. and S. A. N. All the authors discussed the results. The paper was written by Z. P. with feedback from all authors. The project was supervised by J. C., M. A., and Y. W. L.

Data availability

All data needed to evaluate the conclusions in the paper are present in the paper and/or the ESI.†

Conflicts of interest

The authors declare that they have no competing interests.

Acknowledgements

This work was partially supported by the National Natural Science Foundation of China (Grant No. 22271309, 12425403, 12261131499, and 11921004), the National Key R&D Program of China (Grant No. 2021YFA1400300), the Grants-in-Aids for Scientific Research 18H05208 and 19H05625 from the Japan Society for the Promotion of Science (JSPS), and the Kanagawa Institute of Industrial Science and Technology. Y.-W. F. acknowledges the computational resources provided by the NYU New York and NYU Shanghai. The synchrotron radiation experiments were performed at SPring-8 with the approval of the Japan Synchrotron Radiation Research Institute (2019A1045 and 2023B1575).

References

1 P. Mohn, *Nature*, 1999, **400**, 18–19.
2 J. Chen, L. Hu, J. X. Deng and X. R. Xing, *Chem. Soc. Rev.*, 2015, **44**, 3522–3567.
3 D. Das, T. Jacobs and L. J. Barbour, *Nat. Mater.*, 2010, **9**, 36–39.
4 T. A. Mary, J. S. O. Evans, T. Vogt and A. W. Sleight, *Science*, 1996, **272**, 90–92.
5 B. K. Greve, K. L. Martin, P. L. Lee, P. J. Chupas, K. W. Chapman and A. P. Wilkinson, *J. Am. Chem. Soc.*, 2010, **132**, 15496–15498.
6 A. L. Goodwin, M. Calleja, M. J. Conterio, M. T. Dove, J. S. O. Evans, D. A. Keen, L. Peters and M. G. Tucker, *Science*, 2008, **319**, 794–797.
7 B. Mortazavi, A. Rajabpour, X. Zhuang, T. Rabczuk and A. V. Shapeev, *Carbon*, 2022, **186**, 501–508.
8 M. van Schilfgaarde, I. A. Abrikosov and B. Johansson, *Nature*, 1999, **400**, 46–49.
9 K. Takenaka and H. Takagi, *Appl. Phys. Lett.*, 2005, **87**, 261902.
10 X. Song, Z. H. Sun, Q. Z. Huang, M. Rettenmayr, X. M. Liu, M. Seyring, G. N. Li, G. H. Rao and F. X. Yin, *Adv. Mater.*, 2011, **23**, 4690–4694.
11 Y. W. Long, N. Hayashi, T. Saito, M. Azuma, S. Muranaka and Y. Shimakawa, *Nature*, 2009, **458**, 60–63.
12 M. Azuma, W. T. Chen, H. Seki, M. Czapski, S. Olga, K. Oka, M. Mizumaki, T. Watanuki, N. Ishimatsu, N. Kawamura, S. Ishiwata, M. G. Trucker, Y. Shimakawa and P. J. Attfield, *Nat. Commun.*, 2011, **2**, 347.
13 T. NIshikubo, T. Imai, Y. Sakai, M. Mizumaki, S. Kawaguchi, N. Oshime, A. Shimada, K. Sugawara, K. Ohwada, A. Machida, T. Watanuki, K. Kurushima, S. Mori, T. Mizokawa and M. Azuma, *Chem. Mater.*, 2023, **35**, 870–878.
14 J. Chen, F. F. Wang, Q. Z. Huang, L. Hu, X. P. Song, J. X. Deng, R. B. Yu and X. R. Xing, *Sci. Rep.*, 2013, **3**, 2458.
15 Z. Pan, J. Chen, X. Jiang, L. Hu, R. Yu, H. Yamamoto, T. Ogata, Y. Hattori, F. Guo, X. A. Fan, Y. Li, G. Li, H. Gu, Y. Ren, Z. Lin, M. Azuma and X. R. Xing, *J. Am. Chem. Soc.*, 2017, **139**, 14865–14868.

16 Y. Rong, M. L. Li, J. Chen, M. Zhou, K. Lin, L. Hu, W. X. Yuan, W. H. Duan, J. X. Deng and X. R. Xing, *Phys. Chem. Chem. Phys.*, 2016, **18**, 6247–6251.
17 C. S. Coates and A. L. Goodwin, *Mater. Horiz.*, 2019, **6**, 211–218.
18 S. C. Abrahams, S. K. Kurtz and P. B. Jamieson, *Phys. Rev.*, 1968, **172**, 551–553.
19 J. Chen, X. R. Xing, R. B. Yu and G. R. Liu, *J. Am. Ceram. Soc.*, 2005, **88**, 1356–1358.
20 J. Chen, L. L. Fan, Y. Ren, Z. Pan, J. X. Deng, R. B. Yu and X. R. Xing, *Phys. Rev. Lett.*, 2013, **110**, 115901.
21 Z. H. Ren, R. Y. Zhao, X. Chen, M. Li, X. Li, H. Tian, Z. Zhang and G. R. Han, *Nat. Commun.*, 2018, **9**, 1.
22 Z. Pan, Y.-W. Fang, T. Nishikubo, L. Hu, S. Kawaguchi and M. Azuma, *Chem. Mater.*, 2022, **34**, 2798–2803.
23 J. Chen, X. Xing, R. Yu and G. Liu, *Appl. Phys. Lett.*, 2005, **87**, 231915.
24 T. Yang, Y. Wang, L. Fan, N. Wang, K. Lin, J. Chen and X. Xing, *J. Phys. Chem. C*, 2020, **124**, 20445–20449.
25 J. Chen, X. Xing, G. Liu, J. Li and Y. Liu, *Appl. Phys. Lett.*, 2006, **89**, 101914.
26 C. Sun, Z. Cao, J. Chen, R. Yu, X. Sun, P. Hu, G. Liu and X. Xing, *Phys. Status Solidi*, 2008, **245**, 2520–2523.
27 P. Hu, J. Chen, J. Deng and X. Xing, *J. Am. Chem. Soc.*, 2010, **132**, 1925–1928.
28 X. R. Xing, J. Chen., J. Deng and G. Liu, *J. Alloys Compd.*, 2003, **360**, 286–289.
29 Z. Pan, Z. Liang, X. Wang, Y.-W. Fang, X. Ye, Z. Liu, T. Nishikubo, Y. Sakai, X. Shen, Q. Liu, S. Kawaguchi, F. Zhan, L. Fan, Y. Wang, C. Ma, X. Jiang, Z. Lin, R. Yu, X. Xing, M. Azuma and Y. Long, *Mater. Horiz.*, 2024, **11**, 5394–5401.
30 Y. Kobayashi, O. J. Hernandez, T. Sakaguchi, T. Yajima, T. Roisnel, Y. Tsujimoto, M. Morita, Y. Noda, Y. Mogami, A. Kitada, M. Ohkura, S. Hosokawa, Z. Li, K. Hayashi, Y. Kusano, J. E. Kim, N. Tsuji, A. Fujiwara, Y. Matsushita, K. Yishimura, K. Takegoshi, M. Inoue, M. Takano and H. Kageyama, *Nat. Mater.*, 2012, **11**, 507–511.
31 T. Yajima, A. Kitada, Y. Kobayashi, T. Sakaguchi, G. Bouilly, S. Kasahara, T. Terashima, M. Takano and H. Kageyama, *J. Am. Chem. Soc.*, 2012, **134**, 8782–8785.
32 T. Yajima, F. Takeiri, K. Aidzu, H. Akamatsu, K. Fujita, W. Yoshimune, M. Ohkura, S. M. Lei, V. Gopalan, K. Tanaka, C. M. Brown, M. A. Green, T. Yamamoto, Y. Kobayashi and H. Kageyama, *Nat. Chem.*, 2015, **7**, 1017–1023.
33 G. Burns and B. A. Scott, *Phys. Rev. Lett.*, 1970, **25**, 1191–1194.
34 H. O. Pritchard and H. A. Skinner, *Chem. Rev.*, 1955, **55**, 745–786.
35 J. Chen, X. R. Xing, C. Sun, P. H. Hu, R. B. Yu, X. W. Wang and L. H. Li, *J. Am. Chem. Soc.*, 2008, **130**, 1144–1145.
36 R. E. Cohen, *Nature*, 1992, **358**, 136–138.
37 Y. Kuroiwa, S. Aoyagi, A. Sawada, J. Harada, E. Nishibori, M. Takata and M. Sakata, *Phys. Rev. Lett.*, 2001, **87**, 217601.
38 Y.-W. Fang, H.-C. Ding, W.-Y. Tong, W.-J. Zhu, X. Shen, S.-J. Gong, X.-G. Wang and C.-G. Duan, *Sci. Bull.*, 2015, **60**, 156–181.
39 J. Chen, K. Nittala, J. S. Forrester, J. L. Jones, J. X. Deng, R. B. Yu and X. R. Xing, *J. Am. Chem. Soc.*, 2011, **133**, 11114–11117.
40 G. Shirane, R. Pepinsky and B. C. Frazer, *Acta Cryst.*, 1956, **9**, 131–140.
41 G. Kresse and J. Furthmüller, *Comput. Mater. Sci.*, 1996, **6**, 15–50.
42 G. Kresse and J. Furthmüller, *Phys. Rev. B: Condens. Matter Mater. Phys.*, 1996, **54**, 11169–11186.
43 J. P. Perdew, A. Ruzsinszky, G. I. Csonka, O. A. Vydrov, G. E. Scuseria, L. A. Constantin, X. L. Zhou and K. Burke, *Phys. Rev. Lett.*, 2008, **100**, 136406.
44 E. I. P. Aulesti, P. Aulestia, Y. W. Cheung, Y.-W. Fang, J. F. He, K. Yamaura, K. T. Lai, S. K. Goh and H. H. Chen, *Appl. Phys. Lett.*, 2018, **113**, 012902.
45 Y.-W. Fang and H. Chen, *Commun. Mater.*, 2020, **1**, 1.
46 G. Frenking and S. Shaik, *The Chemical Bond: Fundamental Aspects of Chemical Bonding*, Wiley, 2014.
47 Y.-W. Fang, C. A. Fisher, A. Kuwabara, X. W. Shen, T. Ogawa, H. Moriwake, R. Huang and C.-G. Duan, *Phys. Rev. B*, 2017, **95**, 014111.
48 S. L. Dudarev, G. A. Botton, S. Y. Savrasov, C. J. Humphreys and A. P. Sutton, *Phys. Rev. B: Condens. Matter Mater. Phys.*, 1998, **57**, 1505–1509.